Experimental and theoretical analysis of the temperature dependence of rotational Raman linewidths of oxygen

M. Bérard and P. LallemandJ. P. Cebe and M. Giraud

Citation: The Journal of Chemical Physics **78**, 672 (1983); doi: 10.1063/1.444811
View online: http://dx.doi.org/10.1063/1.444811
View Table of Contents: http://aip.scitation.org/toc/jcp/78/2
Published by the American Institute of Physics

Experimental and theoretical analysis of the temperature dependence of rotational Raman linewidths of oxygen

M. Bérard and P. Lallemand

Laboratoire de Spectroscopie Hertzienne de l'Ecole Normale Supérieure, 24 Rue Lhomond 75231, Paris, Cedex 05, France

J. P. Cebe and M. Giraud

Laboratoire des Interactions Moléculaires, Université de Provence 13997, Marseille, Cedex 13, France
(Received 28 July 1982; accepted 17 September 1982)

This paper is devoted to a detailed study of the self-broadening of rotational Raman lines in oxygen in order to obtain information concerning the anisotropic part of the intermolecular potential using the theory of Smith, Giraud, and Cooper. It first recalls the rotational structure of the energy spectrum of O_2 due to its nonzero electronic spin, and shows that a pure Hund's type *b* coupling scheme is not adequate. Then the experimental setup and data analysis procedure are discussed in detail to justify the accuracy of the results. In this part the presence of a weak background in addition to Lorentzian Raman lines is discussed but without giving a plausible physical origin. The next part extends the theory of Smith, Giraud, and Cooper to the case of a $^3\Sigma$ state. The last part presents the experimental results together with theoretical results obtained with an intermolecular potential derived from that of Mingelgrin and Gordon. It is shown that a very good agreement between theory and experiment can be reached provided one takes a slightly steeper repulsive potential. Finally it is shown that the repulsive anisotropic potential is dominating in the whole temperature range that was studied.

I. INTRODUCTION

Getting information about interaction potentials is the aim of many studies, both theoretical and experimental, in molecular physics.[1] Among all the systems that can be chosen, those involving atoms and linear molecules are the simplest and thus deserve most attention. In fairly low density gases where molecules spend most of their time in free flight, one can get information about the intermolecular potential by a variety of measurements related to various aspects of the collisions that can be considered as separate events. Usually these macroscopic measurements correspond to the average effect of collisions with respect to impact parameter and relative energy, so that it is difficult to extract information upon the potential. Obviously elaborate molecular beam techniques[2] lead to a larger information content, but experimental constraints limit the class of molecules that can be studied. An intermediate stage is to work on a large temperature range, which is a poor man's way to control the relative energy.

Traditionally, one makes bulk measurements, like second virial coefficient or transport coefficients, which are somewhat sensitive to anisotropic intermolecular forces.[3] A more direct way to study these forces is to measure the rotational relaxation by acoustic techniques,[4] and preferably to use techniques that are sensitive to molecular reorientation. Among those, one can study the spectral profile of the depolarized Rayleigh light scattering,[5] the influence of a magnetic field upon transport coefficients,[6] or the optical flow birefringence.[7] One can also perform NMR studies. All those techniques will yield molecular reorientation cross sections that are averaged over the molecular rotational states. To obtain more detailed information one can use spectroscopic techniques[8,9] in which one measures the width of infrared, microwave, or Raman lines as they allow one to separate the contribution of various molecular states. One can also determine state to state cross sections using double resonance methods[10] or laser excited fluorescence.[11] Each method has its own experimental requirements and we cannot apply several of them to a single molecular system in order to get a clear picture of the effect of collisions. Needless to say the theoretical situation is not so much better than the experimental one.[1] A large number of methods to calculate collision cross sections have been developed in the past involving a variety of approximations to control the amount of numerical calculations. This tends to obscure the physics and thus to limit the accuracy of the results. Therefore the problem of testing methods to calculate intermolecular potentials[12] is still a formidable one.

In this paper we shall deal with the pressure broadening of rotational Raman lines of oxygen as a function of temperature (100–400 K) and density (5–40 amagat). This yields detailed results for binary O_2–O_2 collisions. For a number of cases, we have made a detailed analysis of the effect of density and found a linear dependence of the linewidths vs density showing a negligible contribution of three-body collisions. This information will be used as a prerequisite in a forthcoming paper on O_2–rare gas which should be much simpler in terms of theoretical interpretation. The corresponding results will be presented elsewhere.

First we have tried to make a rigorous analysis of the experimental spectral profile to obtain accurate pressure broadening coefficients for many values of the rotational quantum number N, and at several tem-

 0021-9606/83/020672-16$2.10

peratures T. We then compare our data to the results of a semiclassical theory[13] which is neither limited by low order perturbation theory or by too simplified relative trajectories.[14] This theory has already given good results in the case of microwave spectra[15] of oxygen and we shall show that it can yield very good results for Raman lines provided small changes are made in the intermolecular potential.

In Sec. II we shall recall in some detail the spectroscopy of oxygen which differs from that of a simple rigid rotor due to the fact that the electronic ground state of oxygen ($^3\Sigma_g^-$) has an electronic spin of one. We shall explain how we deal with the finite resolution of our instruments which does not allow us to resolve some of the Raman lines. This complication is offset by the fact that oxygen has a large Raman cross section and presents widely separated groups of lines, due to its zero nuclear spin leading to the suppression[16] of the even values of N. With nitrogen, that we shall discuss elsewhere, and CO and NO, it is the simplest diatomics, once we set apart H_2, HD, and D_2 which have already been extensively studied.[17]

We describe in Sec. III the experimental setup and the procedure used to analyze the data. We find that the spectrum can be reduced in terms of a series of Lorentzian lines sitting on top of a broad "residual spectrum" whose physical origin we have not been able to find. We shall compare our result to previous ones obtained by Jammu *et al.*[18]

Section IV will recall the semiclassical method of Smith, Giraud, and Cooper,[13] and present its extension to the particular case of oxygen; we shall include new expression for the off-diagonal elements in the relaxation matrix.

Finally, Sec. V will present a comparison of our experimental data with the present theoretical analysis and that of previous authors.[19] We shall test the sensitivity of theoretical calculations to the expression of the intermolecular potential, and suggest a modification of the parameters of the potential used previously for the microwave lines of oxygen.[15]

II. STRUCTURE OF THE ROTATIONAL RAMAN SPECTRUM OF OXYGEN

In order to set the notations used in this paper, and to justify some approximations that will be made, we are going to recall briefly the structure of the rotational Raman spectrum of oxygen.

Within the framework of the polarizability theory of Placzek and Teller,[20] one calculates the rotational Raman spectrum of a gas using the electric dipole $\mathbf{P}=\boldsymbol{\alpha}\mathbf{E}$ which is induced by the incident electric field $\mathbf{E}=\mathbf{E}_0 \times \exp(i\omega_L t)$, assuming that the molecules are uncorrelated to neglect spatial phase factors. The polarizability tensor $\boldsymbol{\alpha}$ for a linear molecule can be decomposed into two tensorial components $\alpha=\alpha_0^{(0)}+\alpha_0^{(2)}$, where

$$\alpha_0^{(0)}=\bar{\alpha}=(2\alpha_\perp+\alpha_\parallel)/3$$

and

$$\alpha_0^{(2)}=\frac{\beta}{3}\begin{pmatrix}-1 & 0 & 0\\ 0 & -1 & 0\\ 0 & 0 & 2\end{pmatrix}$$

with

$$\beta=\alpha_\perp-\alpha_\parallel\ .$$

$\alpha_0^{(0)}$ gives rise to the polarized Rayleigh line (possibly split into the Rayleigh–Brillouin triplet), whereas $\alpha_0^{(2)}$ leads to depolarized inelastic scattering, corresponding to molecular transitions between state $|i\rangle$ and $|f\rangle$. The corresponding lines are centered at $\omega_L+(E_f-E_i)/\hbar$ and their intensity is proportional to the input power, the population of state $|i\rangle$ and the square of the matrix element $\langle i|\alpha_0^{(2)}|f\rangle$.

For a simple linear molecule the rotational states are well known, but in the case of O_2 the existence of an electronic spin $S=1$ in the electronic ground state $^3\Sigma_g^-$ makes matter more complicated. It is frequently assumed that such a state can be described as a Hund's type b coupling[21] whose eigenstates $|N,J,M_J\rangle$ are characterized by the rotational quantum number N (necessarily odd due to the zero value of the nuclear spin) and by the total angular momentum $J=(N-1,\ N,\ N+1)$ due to the coupling of N and S:

$$|N,J,M_J\rangle=(-)^{N-S-M_J}\sqrt{2J+1}\times\sum_{M_N,M_S}\begin{pmatrix}S & N & J\\ M_S & M_N & M_J\end{pmatrix}|N,M_N\rangle\,|S,M_S\rangle\ .$$

However, this coupling scheme leads to intensities for the Raman lines that do not agree with experiment. It is therefore necessary to consider a situation intermediate between Hund's a and b coupling schemes. For a given total angular momentum J, the eigenstates will be

$$\left.\begin{aligned}|+,J,M_J\rangle&=a(J)\,|J+1,J,M_J\rangle+b(J)\,|J-1,J,M_J\rangle\\ |-,J,M_J\rangle&=a(J)\,|J-1,J,M_J\rangle-b(J)\,|J+1,J,M_J\rangle\end{aligned}\right\}\ \text{even } J\ ,$$

$$|0,J,M_J\rangle=|J,J,M_J\rangle\qquad\text{odd } J\ .$$

Table I taken from Ref. 22 gives some values of the coefficients $a(J)$ and $b(J)$. It shows that $a(J)\gg b(J)$ so that using Hund's type b notations is justified. We show, in Table II, the set of transitions that can be found in the Stokes part of the rotational Raman spectrum according to the selection rules $\Delta N=0,\ \pm2$ and $\Delta J=0,\pm1,\pm2$ deduced from the nonvanishing matrix elements of

TABLE I. Coefficients $a(J)$ and $b(J)$ in the intermediate coupling scheme (from Ref. 22).

J	$a(J)$	$b(J)$
2	0.9904	−0.1386
4	0.9971	−0.0766
6	0.9986	−0.0530
...	...	...
20	0.9999	−0.0017
...	...	...
30	0.9999	−0.0011

TABLE II. Positions and intensities of the six allowed Raman transitions $N \rightarrow N+2$. The first line gives the notation, in the Hund's b case terminology. The second and the third give, respectively, the position (in cm^{-1}) and relative intensity for each transition as calculated in Ref. 22. The fourth line gives, when available, the corresponding experimental value for each unresolved line.

N	Unresolved line	$S_-(N)$	$S_0(N)$			$S_+(N)$	
1	Transition	$^3R(1,1)$	$^3Q(2,1)$	$^3S(2,1)$	$^3S(1,1)$	$^3R(2,1)$	$^3S(0,1)$
	Frequency (cm^{-1})	−12.29	−14.17	−14.30	−14.38	−16.25	−16.29
	Relative intensity (%) calc	15.0	1.7	43.9	22.3	8.6	8.6
	Relative intensity (%) expt	14.8 ± 0.5	67.9			17.3 ± 0.5	
3	Transition	$^3R(3,3)$	$^3Q(4,3)$	$^3S(4,3)$	$^3S(3,3)$	$^3S(2,3)$	$^3R(4,3)$
	Frequency (cm^{-1})	−23.86	−25.81	−25.84	−25.87	−25.95	−27.82
	Relative intensity (%) calc	3.9	0.1	39.6	30.0	23.4	2.9
	Relative intensity (%) expt	3.4 ± 0.2	93.9				2.7 ± 0.2
5	Transition	$^3R(5,5)$	$^3S(6,5)$	$^3S(5,5)$	$^3Q(6,5)$	$^3S(4,5)$	$^3R(6,5)$
	Frequency (cm^{-1})	−35.40	−37.34	−37.37	−37.38	−37.41	−39.36
	Relative intensity (%) calc	1.8	27.8	31.8	0.0	27.2	1.4
	Relative intensity (%) expt	1.9 ± 0.2	96.7				1.4 ± 0.2
7	Transition	$^3R(7,7)$	$^3S(8,7)$	$^3S(7,7)$	$^3S(6,7)$	$^3Q(8,7)$	$^3R(8,7)$
	Frequency	−46.91	−48.83	−48.86	−48.88	−48.93	−50.87
	Relative intensity (%) calc	1.0	36.9	32.4	28.9	0.0	0.8
	Relative intensity (%) expt	0.9 ± 0.2	98.4				0.7 ± 0.2
9	Transition	$^3R(9,9)$	$^3S(10,9)$	$^3S(9,9)$	$^3S(8,9)$	$^3Q(10,9)$	$^3R(10,9)$
	Frequency (cm^{-1})	−58.41	−60.31	−60.34	−60.36	−60.45	−62.38
	Relative intensity (%) calc	0.6	36.3	32.7	29.8	0.0	0.6
	Relative intensity (%) expt	?	100.0				?

the irreducible tensorial components of the anisotropic polarizability

$$\langle N, J, M | \alpha_Q^{(2)} | N', J', M' \rangle = (-)^{M-3} \sqrt{5(2J+1)(2J'+1)(2N+1)(2N'+1)/4\pi} \times \begin{pmatrix} J & 2 & J' \\ M & -Q & -M' \end{pmatrix} \begin{pmatrix} 2 & N & N' \\ 0 & 0 & 0 \end{pmatrix} \begin{Bmatrix} N & N' & 2 \\ J' & J & 1 \end{Bmatrix}.$$

For each N, we give the central frequency (in cm^{-1}, relative to ω_L) of the six allowed transitions labeled according to Hund's b case terminology (see Fig. 1). One can see that all these transitions can be grouped to form triplets, that we shall label $S(N)$, each of which being made of three lines, separated by approximately 2.0 cm^{-1} that we shall label $S_-(N)$, $S_0(N)$, and $S_+(N)$, that can be resolved only using very high resolution spectroscopic techniques like CARS. In Table II, for each N, are also reported the theoretical relative intensities of each transition[22] and the corresponding experimental values for each unresolved component.[23] For $N=1$, the three lines have comparable intensities, whereas, for $N \geq 3$, $S_-(N)$, and $S_+(N)$ are only very weak satellites (hardly detectable for $N \geq 11$) and one cannot make a significant analysis of their spectral profile. Note that the depolarized Rayleigh line, which corresponds to the superposition of the transitions $\Delta N = 0$, is equally accompanied by two satellites which make its spectral analysis more complicated. This structure is illustrated by the experimental spectrum of Fig. 2(a) whereas Fig. 2(b) shows how it disappears when the density increases.

The theoretical results that we have briefly recalled here have been compared to experimental data. The relative position of the levels has been studied using high resolution microwave absorption spectroscopy,[24] whereas the intensity of the Raman lines have been compared to accurate experimental data obtained in a previous analysis.[23] The triplet structure will be taken into account here when we analyze the experimental spectra. However we shall perform the theoretical calculations of the line broadening assuming that a pure Hund's type b coupling scheme is valid.

III. EXPERIMENTS

We shall now describe the experimental setup and the techniques used to reduce the data, how we dealt with

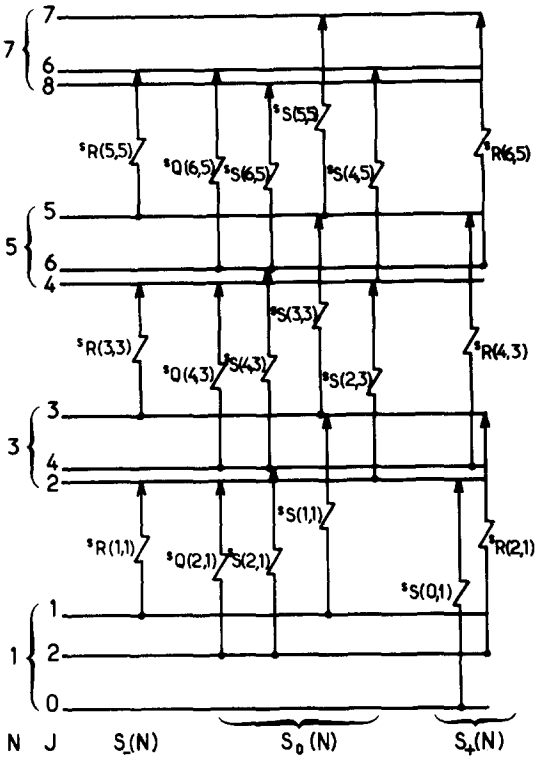

FIG. 1. Energy level diagram of O_2 in the $^3\Sigma_g^-$ state. It shows for $N=1$, 3, 5 the six Raman transitions $(J,N)\rightarrow(J', N+2)$. The vertical energy scale is not linear for clarity. Note the particular arrangement of sublevels corresponding to $N=1$. Note how we group the transitions to form the triplet $\{S_-(N), S_0(N), S_+(N)\}$.

the finite resolution of our instrument, and with the partial overlap of neighboring lines. We shall also discuss possible origins for a broad background that we found assuming that each Raman line is a true Lorentzian.

As indicated in the Introduction, the Raman lines of oxygen are well separated (by about 12 cm^{-1}) and due to their rather high broadening coefficient (about 0.05 cm^{-1}/amagat for the HWHM) one can comfortably work in a density range (5 to 40 amagat) where collision events involving more than two molecules are rare and where the Doppler effect is negligible. Therefore one does not need to use very high resolution spectroscopic techniques like cw CARS.[25] We used a conventional spontaneous Raman scattering equipment that included a few features worth describing in some detail.

A. Experimental setup

The setup we used includes an argon ion laser, a temperature controlled gas cell, and a monochromator followed by a photon counting equipment directly linked to a small computer.

In order to increase the amount of scattered light, we have put the gas cell inside the optical cavity of the laser. This gave us the equivalent of about 25 W at 488 nm. We show in Fig. 3 details of the gas cell which replaced the output mirror of the laser. It includes two highly reflecting spherical mirrors M_1 and M_2 of focal length $f=20$ mm and diameter 8 mm. Mirror M_1 is mounted on an adjustable mount S which allows us to set up the distance $(3f+\epsilon)$ between M_1 and M_2, and thus the radius of curvature f^2/ϵ of the equivalent mirror. To obtain a TEM Gaussian beam with transverse distribution $\exp(-2r^2/w^2)$ when the laser is fitted with a back plane mirror M_0 distant of 2 m, we find that $0.05 < \epsilon < 0.15$ mm. This leads to satisfactory operating conditions. We obtain a waist of 4 μm at the focus in the cell and values of w equal to 2 mm at M_2 and 0, 5 mm at M_0. The angle between the beams reflected by M_1 is 8° in order to avoid vignetting by M_2. To obtain

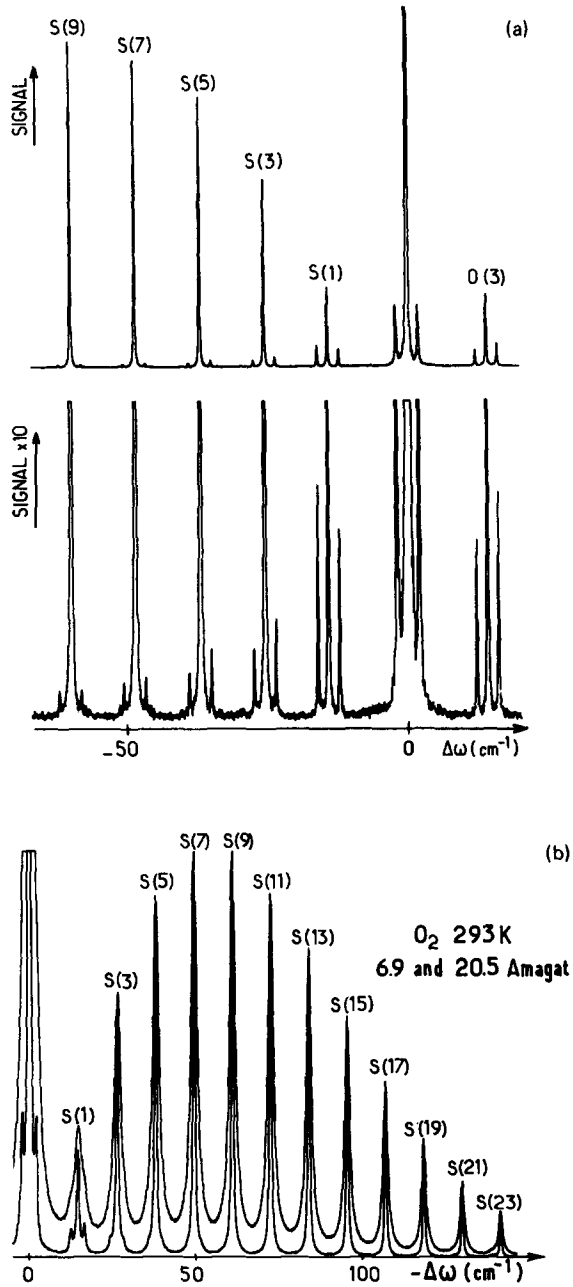

FIG. 2. (a) Rotational Raman spectrum of oxygen (1 atm, 293 K). The satellites can be seen on the lower curve with a ×10 increase in sensitivity. (b) Self-broadening of the rotational Raman spectrum of oxygen.

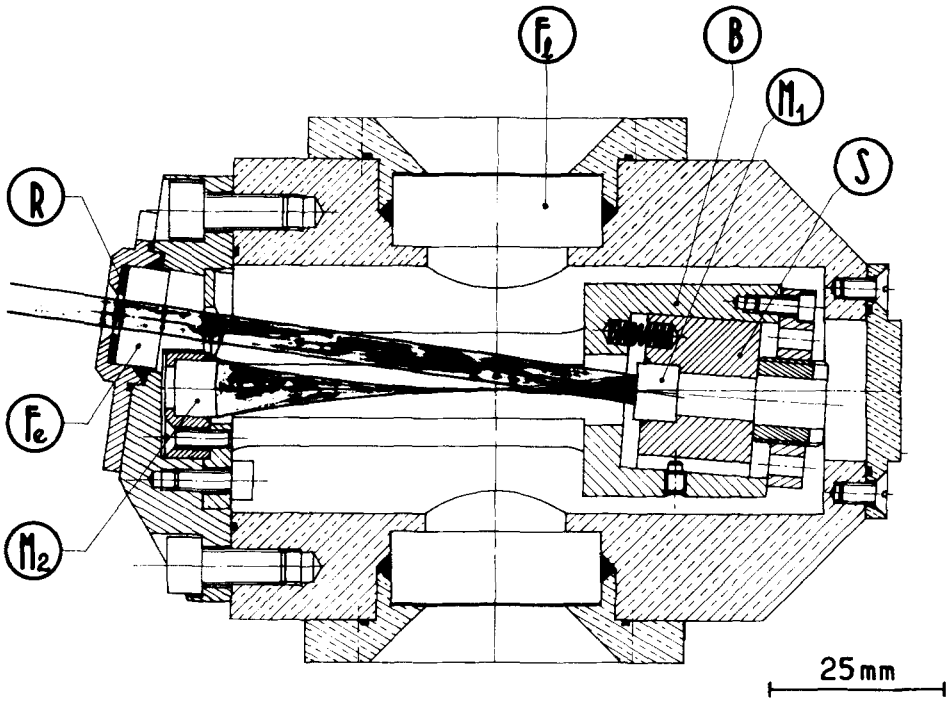

FIG. 3. Details of the intracavity gas cell. Mirror M_1 is placed on an adjustable mount to obtain the required radius of curvature for the equivalent mirror. Optical elements (mirrors M_1 and M_2, input window F_e) are placed on an invar mount.

the correct angular alignment of the laser, the cell and the cryostat in which it is placed can be moved with the required accuracy. The whole laser system was found to be quite stable.

The body of the gas cell is made out of brass to obtain a good thermal equilibrium, but the optical elements (mirrors M_1 and M_2 and the entrance window F_e) are set on an invar bench to keep the laser adjustments when the temperature is changed from room temperature where the initial tuning is made, with due respect of the later dilatation or contraction of the invar to have the maximum power at the operating temperature.

The entrance window F_e is made out of fused silica and, being set perpendicular to the beam, is antireflection coated. This was preferred to a Brewster angle window because only minor readjustments need to be made when the gas pressure is changed. This window is stressed by the internal pressure and becomes birefringent, which may lead to excessive losses in the laser cavity. Special care was thus taken to mount it properly on a polished metal ring R using a soft glue to insure that there is no leak.

To control the temperature of the cell, we put it in a vacuum chamber which requires an additional window in the laser cavity. It is in weak thermal contact with a cold (hot) finger whose temperature is held constant to ± 0.2 °C using a suitable coolant (liquid N_2 around 100 K; cold methanol between 180 K and room temperature; heated oil above). The cell itself is fitted with a heating resistance and a platinum thermometer used in a temperature control loop. The stability is quite good $\sim \pm 0.01$ °C, but the exact value of the temperature T of the gas is not well known due to temperature gradients. The pressure P is measured with a Bourdon type manometer. From P and T, we can determine the density of the gas using its equation of state. We estimate that we know the density with a relative uncertainty of 4% near 100 K, 1% at room temperature and 2% elsewhere. One of the difficulties is that there may be local heating of the gas at the focus of the laser beam and a change in the actual temperature over that of the metallic cell. It turns out that in some cases we have observed turbulent motions of the gas when the beam is not well centered on the mirrors, due to the presence of hot spots. Only on such occassions would the scattered light intensity be affected so that we discarded the corresponding data. Furthermore, if we operate the laser at 476.5 nm we observe a strong defocusing of the beam which leads to a severe reduction in laser power. This is due to an absorption of $(O_2)_2$ transient molecules which does not occur at our usual operating wavelength of 488 nm. In principle one could obtain a direct measurement of the temperature of the gas which is located in the laser beam by measuring the Stokes/anti-Stokes intensity ratio for large N lines. But to get the required accuracy, one needs a very stable laser and a precise calibration of the detection system. In addition when there is some overlap of the lines, which often occurs under our operating conditions, it is very hard to extract precise values for the intensity of each spectral line. We therefore did not try to use this optical probe for the gas temperature.

The collection of the scattered light is done at 90° of the incident beam (between M_1 and M_2), using a lens with focal length 75 mm and $f/1.7$ aperture. This lens is located such that the waist of the laser is imaged with magnification of five on the slit of the spectrometer. Usually the entrance slit is 15 μm wide and 10 mm high and the angular aperture of the monochromator is $f/10$ parallel to the slit and $f/20$ perpendicular to it. Therefore the solid angle in the cell is $\Omega = 0.12$ sr. As

a result some polarized Rayleigh scattered light gets into the monochromator even though we chose the polarization of the laser beam such that it is minimum. Using the standard notation for Raman spectroscopy, where V and H mean, respectively, that the polarization is perpendicular or parallel to the scattering plane, we chose to detect $(I_{HH}+I_{HV})$. Knowing the observation solid angle and the polarizability tensor components of oxygen, we find calling I_{RAY} the total polarized Rayleigh intensity and I_{RAM} the total depolarized Raman intensity detected, that we have

$$\frac{I_{RAY}}{I_{RAM}} \simeq \frac{15}{4\pi}\left(\frac{\bar{\alpha}}{\beta}\right)^2 \Omega \simeq 30\% .$$

Of course, the power spectral density for $\omega = \omega_L$ is obviously much larger than the maximum power density for Raman lines, because I_{RAY} is concentrated in a very narrow spectral range.

The superposition of polarized and depolarized components near $\omega = \omega_L$ with a not well known ratio is one of the reasons why we do not analyze the central component. To do this properly requires one to take a much smaller solid angle and to use a higher resolution instrument like a Fabry Perot interferometer.[5(a),5(b)] The spectral analysis is performed using a grating monochromator Jarell–Ash model 25–100 of 1 m focal length fitted with a single 300 lines/mm echelon grating. We operate the instrument in the 11th order which corresponds to the blaze angle of the grating. With entrance and output slits 15 μm wide and 10 mm high, the polarized Rayleigh scattering by low pressure argon leads to a line 0.2 cm^{-1} (FWHM) wide. This value is due to an unknown combination of Doppler broadening, spectrometer resolution and laser line broadening (we did not attempt to select a single longitudinal mode of the laser as the presence of the cell in the cavity made it too unstable as far as mode hopping is concerned).

The final detection was done using a R 464 Hamamatsu photomultiplier followed by photon counting equipment. Typical counting periods were 0.5 s and a whole spectrum included about 3000 points. These 3000 photocounts were then transferred into a Heathkit H11A microcomputer for data processing.

B. Analysis of the spectra

We shall now describe how we analyze the data using a piecewise method to determine the width of each component. At room temperature and above we usually analyze 14 sets of triplets $S(N)$ $(1 \leq N \leq 27)$, while at 100 K we limit ourselves to $N \leq 15$.

The experimental spectra or records contain from 1800 to 3000 numbers corresponding to the integral of the power spectral density over an interval $\delta\omega = 0.06$ cm^{-1}. This interval is very small compared to the separation of two lines $(8B_0 = 11.5\ cm^{-1})$ and small compared to width of a line (typically 2 cm^{-1} FWHM for 20 amagat) which is itself large compared to the instrumental band pass.

Contrary to previous investigators[18,26] who studied this kind of spectra, we have tried to use the whole amount of information contained in a record. Now instead of making a multiparameter analysis of the data by comparing it directly to the exact formula for the complete Raman spectrum [Eq. (IV.5) to be presented in Sec. IV of this paper], we have analyzed it as a sum of Lorentzian components together with a broad and slowly varying background. This procedure will be justified *a posteriori* by the excellent fit that it allows us to achieve.

In the density range at which we have worked (typically 20 amagat), the influence of the instrumental resolution is quite small. We assumed that all the lines of the spectrum are Lorentzian and that the convolution by the slit function just broadens them but without changing their shape. This would be exact if the slit function was itself Lorentzian. We shall explain later how we dealt with this problem. Now there is always some partial overlap of neighboring lines which ought to prevent a piecewise analysis. To get around this difficulty we used the following iteration scheme.

We first isolate around each line or triplet $S(N)$ a part of the spectrum including $4B_0/\delta\omega = 90$ spectral elements on either side of the center of $S_0(N)$. In the first step, we assume that the wings of the neighboring lines can be replaced by a constant contribution $a(N)$, so that the data will be used to determine $a(N)$ and the parameters of $S_0(N)$ if $N > 9$ or $a(N)$ and the parameters of the triplet $S(N) = \{S_-(N), S_0(N), S_+(N)\}$ with the help of a simple method to be described later. This allows us to obtain a first set of experimental results (heights, widths, and positions). In the next step we analyze each line in the same way but after subtracting the wings that can be calculated with the set of results. This process can be repeated several times. It turns out that it converges quite fast unless the lines are so broad that there are only shallow minima between successive maxima. Typically three iterations are sufficient.

We have found systematically that a background $a(N)$ remains when the iteration is completed. This background increases with the density but its origin is not known as we shall discuss later. It is however necessary to include it to get a good fit between data and reconstructed spectra. As an example we show in Fig. 4 the best fit assuming $a(N) = 0$ and compare it to that obtained for $a(N) \neq 0$.

The procedure that we outlined above involves the analysis of a large number of Lorentzian lines. It was therefore worthwhile looking for a fast way to do it, as a standard least square fitting procedure led to unacceptably long computations with the equipment we have. We shall first explain how we analyze an isolated line, with possible small satellite $(3 \leq N \leq 9)$. We shall deal afterwards with the $S(1)$ triplet.

C. Fast analysis of one line $(N \geq 3)$

Let us, for the moment, forget the presence of the weak satellites $S_-(N)$ and $S_+(N)$ to concentrate on $S_0(N)$. We possess $2P = 8B_0/\delta\omega = 180$ photocounts that constitute the raw information from which we want to extract but a few numbers. This local record

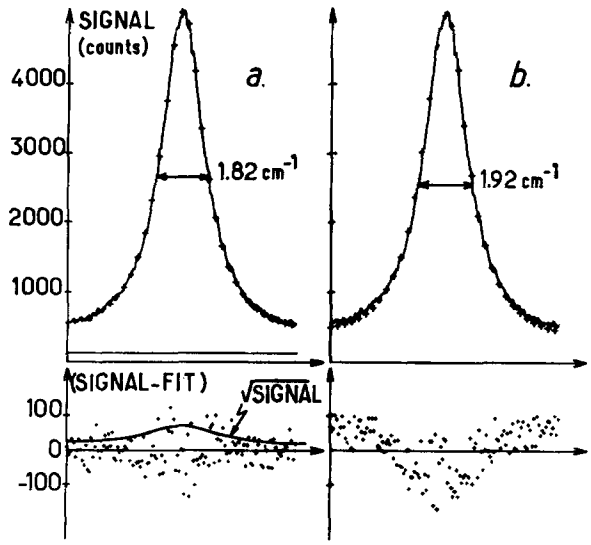

FIG. 4. The upper part shows a comparison of experimental signals (—) with best fits to a Lorentzian; (a) With background, (b) without background. The lower part shows the corresponding deviations. Case (b) shows systematic deviations, while case (a) can be attributed to shot noise.

$\{\phi(n\delta\omega);\ n = L_N + 1, \ldots, L_N + 2P\}$ corresponds to a Lorentzian curve:

$$f(n\delta\omega) = a + h\left[1 + \left(\frac{n\delta\omega - c}{\gamma}\right)^2\right]^{-1},$$

but each photocount is affected by noise. If we assume that the experimental setup is stable during the time necessary to obtain the record, then in principle, the only source of noise is the statistical nature of the photon counting process which leads to shot noise $b(n)$.

As discussed elsewhere[27] the statistical properties of shot noise $\langle b(n)\rangle = 0$; $\langle b(n)\, b(m)\rangle = \delta_{n,m}\langle\phi(n\delta\omega)\rangle$, lead to the most probable values of the parameters (a, h, γ, c) by minimizing the quantity

$$\sum_n [\phi(n\delta\omega) - f(n\delta\omega)]^2 / f(n\delta\omega). \qquad \text{(III.1)}$$

This is the least square method with appropriate weighting factors to take into account the particular properties of shot noise.

Instead of using Eq. (1) which is nonlinear both in c and γ, we have used a fast algorithm in which we use three partial sums over the record: one near the center, one near the wings, and the total integrated spectrum, after determining approximately where the center of the line is. In Ref. 27 we explain in detail how we proceed and calculate analytically the statistical dispersion on the determination of γ over many records differing only in the noise component $\{b(n)\}$. We show that this dispersion $\Delta\gamma = \sqrt{\langle\gamma^2\rangle - \langle\gamma\rangle^2}$ is found to be only slightly larger than that given in the standard square fitting when we simulate a large series of records.

When we study the analytical expression for the dispersion $\Delta\gamma$, we find that it is proportional to $(Ph)^{-1/2}$, that it increases with a/h (because a larger asymptote a leads to an increase in noise), and that it is minimum, all being equal, when

$$0.15 \lesssim \gamma/P\delta\omega \lesssim 0.25 .$$

This fits with physical sense, because for small $\gamma/P\delta\omega$ we have little information about the Lorentzian and for large $\gamma/P\delta\omega$ only $a+h$ is well known.

In our case $P\delta\omega = 4B_0 \simeq 6$ cm^{-1}, so that the best precision will be obtained for $\gamma \simeq 2$ cm^{-1} which is the typical value that we obtain at almost 40 amagat. For $a/h \simeq 1$ one gets theoretically $\Delta\gamma/\gamma = 6/\sqrt{Ph}$. Thus the relative theoretical accuracy is 2% for $h = 1000$ counts/channel.

Figure 4, which we presented to show the necessity of including a nonzero background, includes a comparison of the noise (data fit) with the square root of the fit. This gives an idea about the fact that the noise follows the usual assumptions made about shot noise.

Now we can take care of the small satellites $S_-(N)$ and $S_+(N)$. We know their relative position and intensity and we assume that they have the same width as $S_0(N)$. This allows us to subtract their contributions to be left with a single Lorentzian in our iterative way for $S_0(N)$.

D. Analysis of the $S(1)$ triplet

As the three components of the $S(1)$ triplet have comparable intensities and are quite close to one another, it is not possible to separate them as soon as the density is larger than about 10 amagat. This leads us to analyze this triplet in more detail than other parts of the spectrum. In a preliminary study,[23] we made a detailed analysis of eight spectra obtained at room temperature at densities less than 15 amagat. We found that it was not necessary to take into account off-diagonal elements in the relaxation matrix so that, even with a large overlap of the lines, the spectrum can be represented by a sum of three separate Lorentzian lines convoluted by the instrumental function. This result has been confirmed by a theoretical calculation of the diagonal and off-diagonal elements of the relaxation matrix.[28]

From this study, we assumed that we could analyze the $S(1)$ triplet over the whole range of experimental conditions of the present work, by a sum of three Lorentzian of the same width and with intensity ratio given in Table II. This procedure may affect the accuracy of our results for the broadening coefficient of the $S(1)$ line but in a way much smaller than that due to the strong wings of the central depolarized Rayleigh components.

E. Effect of the instrumental resolution

As our setup led to an instrumental resolution of 0.2 cm^{-1} FWHM, due to Doppler effect, laser linewidth and monochromator resolution, which is about an order of magnitude smaller than the typical widths of the lines we studied, we did not need to deconvolute the data before analyzing it. Instead we proceeded in the following way: We took a series of calculated Lorentzian lines of width γ_{re} and convoluted them by the instrumental function. We then analyzed the simulated lines using the method described above, which yields a width γ_{ap}.

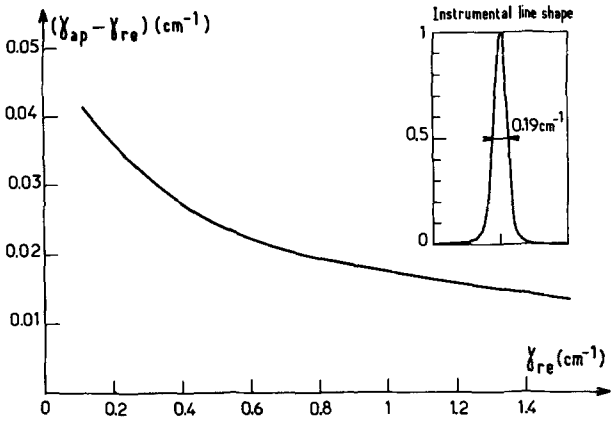

FIG. 5. Correction to be made to the data analysis in order to take the instrumental resolution (0.19 cm^{-1} FWHM) into account.

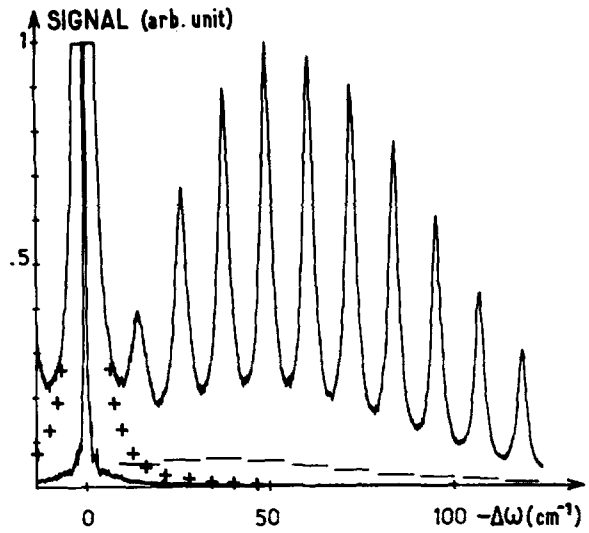

FIG. 6. Possible origins of the experimental background. We compare the depolarized Raman cross section of oxygen and argon for 293 K and 38.5 bar, with appropriate scaling of the instrumental sensitivity. This shows that collision induced light scattering is not responsible for the background. We also show (+) the estimated wing of the central depolarized Rayleigh component of oxygen.

This led us to a relationship $\gamma_{ap}(\gamma_{re})$. We show in Fig. 5 the difference between γ_{ap} and γ_{re}. As most of our data corresponded to a width $\gamma_{re} \gtrsim 1$ cm^{-1}, this shows that the correction is of the order of 2% and that one may neglect the uncertainties due to this process. It should be noted that this way of dealing with the experimental data is consistent.

F. Residual spectrum

We have discussed in Sec. III B how we were led to analyze our experimental data in terms of a sum of independent Lorentzian lines together with a slowly variable "residual spectrum," whose value is equal to the background that is left after completing the iteration scheme described in Sec. III B. Figure 6 shows an example of the corresponding contributions. Now even if this way of describing the data leads to reproducible results, it should be questioned. At this stage we can only repeat that assuming purely Lorentzian lines without background leads to a poor fit as shown in Fig. 4.

We tried to find an explanation for this background.

(1) It is not due to collision induced light scattering. This process is well known in rare gases or in optically isotropic molecules where it leads to a broad featureless depolarized spectrum centered at the laser frequency with an intensity proportional to the square of the density at least when higher than two body collisions are negligible. In a separate study,[29] we calculated the corresponding spectrum in the case of two colliding linear molecules. It shows that in the spectral region of the most intense rotational Raman lines, light scattering due to collision induced processes would be at most 1% of the rotational Raman scattering. To confirm this prediction, at least indirectly, we recorded successively spectra of oxygen and argon for the same density and experimental conditions. As these molecules have similar values for the isotropic polarizability and their Lennard-Jones diameter, the collision induced light scattering should be comparable. Figure 6 shows that, at least outside a 20 cm^{-1} spectral range around the Rayleigh line, collision induced light scattering can be neglected.

(2) It is not due to stray light or ghosts of our spectrometer. If we fill the cell with helium, and make suitable changes in the recording scale to get comparable intensities at the center of the Rayleigh line, we find a negligible background. We recall that in helium the collision induced spectrum is extremely weak.[30]

(3) Now we may question the way in which we take into account the wings of the depolarized Rayleigh component. This line is very intense as it includes almost 1/4 of the total depolarized intensity and its shape is known not to be Lorentzian.[5]

We indicated in Secs. II and III A that we did not attempt to analyze in any detail the central component in our spectra because of its satellites, and as it is a sum of a true depolarized component and of a polarized component with an unknown intensity ratio. We proceeded in the following way: Once we had a good determination of the intensities of the rotational Raman lines $S(N)$ and their widths $\gamma(N)$, we calculated the intensity I_{DR} of the central depolarized line using the general expression for the spectrum. In order to estimate its width γ_{DR}, we usually took an average value of $\gamma(N)$ with weights corresponding to the intensity of the depolarized Q branch for the triplet N. The value obtained in this way is probably too large. It turns out that for room temperature, where it has been measured directly, the true width of the depolarized central component[7(a)] is about equal to 50% of the value obtained by direct reference to the rotational Raman lines.

We have verified however that the uncertainty on the width of the central line has only a small effect on the determination of the widths of the S lines, provided we work at low enough pressure. If we consider a spectrum registered at 40 amagat, for room temperature,

where the S lines are about 4 cm^{-1} wide, a reduction of 50% in the value of γ_{DR} from the average value referred to above, leads to a reduction of approximately 5% for $\gamma(1)$ and 1% for $\gamma(3)$, with a negligible effect for other lines. This shows that our way of processing the data is not sensitive to the details of the central line. Now even for the widest value γ_{DR}, the corresponding wings decay quite rapidly and therefore cannot account for the residual spectrum that we observe for $N > 7$ (see Fig. 6). Note that this argument fails if the central component is non-Lorentzian with a large increase of the intensity in the wings.

From these arguments, one can say that the residual spectrum is probably due to a true Raman scattering process. We can only give an approximate shape for low frequencies ($\omega - \omega_L < 20 B_0$), due to a poor knowledge of the wings of the central component. The corresponding spectral profile shown in Fig. 6 does not depend upon the density of the gas, at least in the pressure range of the present experiments. Its intensity varies nonlinearly with the density, but somewhat less rapidly than the square of the density.

Finally, the effect of overlap of neighboring lines has been considered first by analyzing in detail the $S(1)$ triplet in Ref. 23, and then by introducing nonzero off-diagonal terms in the relaxation matrix. We found that it was not possible to get a good fit to the data by this method, even taking off-diagonal elements much larger than those calculated in Ref. 28.

For want of a satisfactory explanation, we can only say that it comes from the fact that the rotational Raman lines differ from a true Lorentzian line shape, with an increase of intensity in the near wings. If this corresponds to a general effect, it should be studied in molecules, like H_2 or HCl whose Raman lines are spaced by a much larger value than in oxygen in order to determine its true spectral shape. One might then observe in Raman scattering the same kind of deformation of the line wings as is done in infrared spectroscopy, where similar effects are encountered and interpreted as being due to the finite duration of molecular collisions.[31]

G. Comparison with earlier experimental results

The most extensive work related to Raman line broadening in oxygen is that of Jammu *et al.*[18] performed in prelaser days and at room temperature. We compare their results with ours in Fig. 7. The important differences that we find are probably due to the resolutions of the instrument used by the Canadian group and to the techniques used to derive linewidths from their photographic plates.

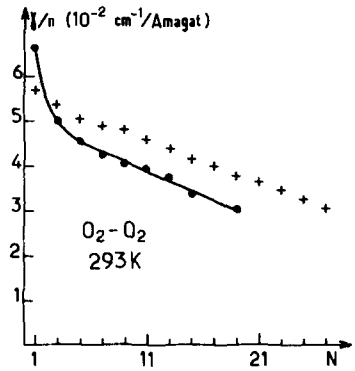

FIG. 7. Comparison of the present experimental results (+) with those of Jammu *et al.* (•••) (Ref. 18).

IV. THEORY OF RAMAN LINE SHAPES

We shall recall briefly how one can calculate Raman linewidths and indicate which approximations have been made here.

A. General features

If one considers the case of an active molecule in a thermal bath of perturbers, one can show[32] that the spectral function of the nonresonant depolarized Raman scattering is proportional to the real part of the Fourier transform of the correlation function of the relevant molecular polarizability tensor component

$$F(\omega) = \mathrm{Re} \int_{-\infty}^{\infty} dt\, e^{i\omega t} \langle \alpha(0)\, \alpha(t) \rangle \,. \tag{IV.1}$$

In the above expression the frequency $\omega = \omega_S - \omega_L$ is the difference between the scattered and the input laser frequencies.

The Liouville space formalism, developed by Fano,[33] is well adapted to obtain a general expression for the spectral function

$$F(\omega) \propto \mathrm{Im\,Tr}\{\alpha(0)\,(\omega - L)^{-1} \rho\, \alpha(0)\}\,, \tag{IV.2}$$

where L is the sum of three Liouvillians $L_0^{(r)}$, $L_0^{(b)}$, and L, associated, respectively, with the Hamiltonian of the active molecule, the bath of perturbers and the molecular interactions. ρ is the density matrix which can be factorized as a product of density matrices describing the bath and the active system $\rho = \rho^{(r)} \rho^{(b)}$, when there is no initial correlation between the two. Taking a partial trace over the bath, we can write

$$F(\omega) = \mathrm{Im\,Tr}_{(r)} (\alpha(0) \{\omega - L_0^{(r)} - \mathrm{Tr}_{(b)} [\rho^{(b)} R(\omega)]\}^{-1} \rho^{(r)}\, \alpha(0))\,, \tag{IV.3}$$

where we define $R(\omega)$ as the relaxation matrix of the system.

The trace of the operator $\rho^{(b)} R(\omega)$ cannot be performed in the general case. This difficulty may be resolved in the impact approximation which applies if the collision time is very short compared to the mean time between collisions or any time of interest for the phenomenon under study. With this assumption, one can show[9,34,35] in the classical path approximation, that the trace over the bath of the relaxation operator is linear in the density of perturbers and has negligible ω dependence. This leads to

$$\begin{aligned} \bar{R} &= \mathrm{Tr}_{(b)} \{\rho^{(b)} R\} \\ &= -2\pi i n \int_0^{\infty} b\, db \int_0^{\infty} v\, dv\, f(v)(1 - S) \\ &= -i n \langle v \sigma(v) \rangle_v \,, \end{aligned} \tag{IV.4}$$

where n is the density of perturbers, b is the impact parameter in binary collisions, v is the relative velocity of the colliding system, $f(v)$ is the Maxwellian distribution of relative velocity, and S is the scattering operator in Liouville space.

In the absence of an external field, the total Hamiltonian is invariant under rotation. Thus substituting Eq. (IV.4) into Eq. (IV.3) one can write Eq. (IV.3) in a rotationally invariant form using the reduced Liouville vectors

$$F(\omega) = -\operatorname{Im}\left\{\sum \langle N_i' J_i' \| \alpha \| N_f' J_f' \rangle \times [\omega - L_0^{(r)} - \bar{R}]^{-1}_{N_i' J_i' N_f' J_f'; N_i J_i N_f J_f} \rho^{(r)}_{N_i J_i} \langle N_i J_i \| \alpha \| N_f J_f \rangle\right\}, \tag{IV.5}$$

where $\sum$ means a summation over all quantum numbers subject to the selection rules. In the preceding expression

$$\bar{R} = -in \int_0^\infty v\sigma(v) f(v)\, dv \tag{IV.6}$$

with

$$\sigma_{N_i' J_i' N_f' J_f'; N_i J_i N_f J_f}(v) = 2\pi \int_0^\infty b\, db \left\{ \sum_{\substack{m_i m_i' \\ m_f m_f' \\ Q}} (-1)^{J_i - J_i' + m_i - m_i'} \begin{pmatrix} J_i' & J_f' & 2 \\ -m_i' & m_f' & Q \end{pmatrix} \begin{pmatrix} J_i & J_f & 2 \\ -m_i & m_f & Q \end{pmatrix} \times [\Delta - \langle N_i' J_i' m_i' | S | N_i J_i m_i \rangle \langle N_f' J_f' m_f' | S | N_f J_f m_f \rangle^*] \right\}, \tag{IV.7}$$

with $\Delta = \delta_{N_i' N_i}\, \delta_{N_f' N_f}\, \delta_{J_i' J_i}\, \delta_{J_f' J_f}$.

One can note that the spectrum will not be a simple sum of Lorentzian corresponding to each allowed Raman transition when the off-diagonal elements of the relaxation operator are significant.

B. Semiclassical calculation of the S matrix for the oxygen molecule

We shall use a semiclassical theory which has been described in detail in Refs. 13 and 15. We determine the exact classical trajectories of the colliding system using the spherically symmetric part of the intermolecular potential. This potential is expressed as

$$V(r, \theta) = V_0(r) + \sum_{l>0} V_l(r) P_l(\cos\theta), \tag{IV.8}$$

where r is the distance between the centers of mass of oxygen and the perturber, θ the angle between the axis of the O_2 molecular and the vector joining the centers of mass. P_l is a Legendre polynomial of order l. Clearly this potential does not involve the internal structure of the perturber and this may be a serious limitation to be discussed later. Note that we have not explicitly included the quadrupole–quadrupole potential which varies as r^{-5}. For $r \sim \sigma$ it is of the same order of magnitude as $V_{att}(r)$ that we shall consider later [Eq. (IV.23)], and becomes larger at large r. However, the discussion of Sec. V will show that in practice only the repulsive part of the potential $V_{rep}(r)$ plays a role so that neglecting a long range contribution to the potential was allowed.

We write the S matrix in exponential form

$$S = \mathcal{O} \exp i\eta, \tag{IV.9}$$

where $\mathcal{O}$ is the ordering operator and η is the phase integral defined by its elements in the rotational molecular states

$$\langle NJm | \eta | N'J'm' \rangle = \int_{-\infty}^{\infty} dt \exp(i\omega_{NJ, N'J'} t) \times \langle NJm | \sum_{l>0} V_l[r(t)] P_l[\cos\theta(t)] | N'J'm' \rangle. \tag{IV.10}$$

To calculate those matrix elements we shall use the peaking approximation in which one neglects the rotation of the intermolecular axis, thus $\theta(t) = \theta_0$. Developing the Legendre polynomials in spherical harmonics and taking into account the rotational invariance of $\sigma(v)$ we can write:

$$\langle NJm | \eta | N'J'm' \rangle = 2\delta_{mm'} \sum_{l>0} \sqrt{\frac{4\pi}{2l+1}} \langle NJm | Y_0^l(\Omega) | N'J'm \rangle \times \int_0^\infty \cos(\omega_{NJ, N'J'} t)\, V_l[r(t)]\, dt. \tag{IV.11}$$

The above expression shows that the peaking approximation implies that the orientation of the total molecular angular momentum does not change with respect to the colliding frame. We shall discuss later this approximation.

We can then expand S

$$\langle NJm | S | N'J'm \rangle = 1 - i \langle NJm | \eta | N'J'm \rangle + \sum_{n\geq 2} \frac{I_n}{n!}, \tag{IV.12}$$

where

$$I_n = (-i)^n \sum_{\substack{J_2 N_2 \\ \cdots \\ J_n N_n}} \langle NJm | \eta | J_2 N_2 m \rangle \cdots \langle N_n J_n m | \eta | N'J'm \rangle$$

and make the central approximation of our theory

$$\langle NJm | \eta | N'J'm \rangle = \eta_{\Delta J, \Delta N}, \tag{IV.13}$$

where $\Delta J = J' - J$ and $\Delta N = N' - N$.

This allows us to calculate the terms in Eq. (IV.12). Following Ref. 15, we obtain a general expression for the matrix elements of S as a sum of products of Bessel functions

$$\langle NJm|S|N'J'm\rangle = e^{-i\eta_{00}}[J_0(A_{10})J_0(A_{20})J_0(A_{02})J_0(A_{12})J_0(A_{22})\delta_{\Delta N,0}\delta_{\Delta J,0}] + \delta_{\Delta N,0}\sum_{k>0} i^k J_k(A_{10})(e^{-\alpha_{10}}\delta_{-\Delta J,k} + e^{\alpha_{10}}\delta_{\Delta J,k})$$

$$\times\left\{\prod_{\substack{i\neq1\\ j\neq0}} J_0(A_{ij})\right\} + \delta_{\Delta N,0}\sum_{l>0} i^l J_l(A_{20})(e^{-\alpha_{20}}\delta_{-\Delta J,2l} + e^{\alpha_{20}}\delta_{\Delta J,2l})\left\{\prod_{\substack{i\neq2\\ j\neq0}} J_0(A_{ij})\right\} + \delta_{\Delta J,0}\sum_{m>0} i^m J_m(A_{02})(e^{-\alpha_{02}}\delta_{-\Delta N,2m}$$

$$+ e^{\alpha_{02}}\delta_{\Delta N,2m})\left\{\prod_{\substack{i\neq0\\ j\neq2}} J_0(A_{ij})\right\} + \sum_{n>0} i^n J_n(A_{12})(e^{-\alpha_{12}}\delta_{-\Delta J,n}\delta_{-\Delta N,2n} + e^{\alpha_{12}}\delta_{\Delta J,n}\delta_{\Delta N,2n})\left\{\prod_{\substack{i\neq1\\ j\neq2}} J_0(A_{ij})\right\} + \sum_{p>0} i^p J_p(A_{22})(e^{-\alpha_{22}}\delta_{-\Delta J,2p}$$

$$\times\delta_{-\Delta N,2p} + e^{\alpha_{22}}\delta_{\Delta J,2p}\delta_{\Delta N,2p})\left\{\prod_{\substack{i\neq2\\ j\neq2}} J_0(A_{ij})\right\} + \text{higher order terms}\ . \qquad \text{(IV.14)}$$

In this expression J_r is a Bessel function of order r,

$$A_{rs} = 2(\eta_{rs}\eta_{-r-s})^{1/2}$$

and

$$\alpha_{rs} = th^{-1}\left[\frac{\eta_{rs}-\eta_{-r-s}}{\eta_{rs}+\eta_{-r-s}}\right]\ . \qquad \text{(IV.15)}$$

The first term of Eq. (IV.14) generalizes the results obtained previously to a $^3\Sigma$ state. It will be used when calculating the width of isolated lines. The other terms are relevant for the calculation of the off-diagonal matrix elements of R. Therefore they will be needed only when strong overlap of the spectral lines occurs.

We can now use these results to determine the half-width at half-height of an *isolated* depolarized rotational Raman line. Using Eq. (IV.5) we get

$$\gamma_{N_iJ_i,N_fJ_f} = -2\pi\,\mathrm{Im}(\bar{R}) = 2\pi n\int_0^\infty vf(v)\,dv\int_0^\infty b\,db$$

$$\times\left[1 - \mathrm{Re}\sum_{\substack{m_i m_f\\ Q}}\begin{pmatrix} J_i & J_f & 2\\ -m_i & m_f & Q\end{pmatrix}^2\right.$$

$$\left.\times\langle N_iJ_im_i|S|N_iJ_im_i\rangle\langle N_fJ_fm_f|S|N_fJ_fm_f\rangle^*\right]\ . \qquad \text{(IV.16)}$$

This can be split into two contributions:

$$\gamma_{N_iJ_i,N_fJ_f} = \gamma^{in}_{N_iJ_i,N_fJ_f} + \gamma^{el}_{N_iJ_i,N_fJ_f} \qquad \text{(IV.17)}$$

with

$$\gamma^{in}_{N_iJ_i,N_fJ_f} = \tfrac{1}{2}(\gamma^{in}_{N_iJ_i} + \gamma^{in}_{N_fJ_f})\ ,$$

where $\gamma^{in}_{N,J}$ is the total inelastic rate out of level N, J

$$\gamma^{in}_{N,J} = 2\pi n\int_0^\infty vf(v)\,dv\int_0^\infty b\,db$$

$$\times\sum_m\frac{1}{2J+1}[1 - |\langle NJm|S|NJm\rangle|^2]\ . \qquad \text{(IV.18)}$$

Similarly the elastic contribution to the linewidth is given by

$$\gamma^{el}_{N_iJ_i,N_fJ_f} = -\pi n\int_0^\infty vf(v)\,dv\int_0^\infty b\,db$$

$$\times\sum_{\substack{m_i m_f\\ Q}}\begin{pmatrix} J_i & J_f & 2\\ -m_i & m_f & Q\end{pmatrix}^2$$

$$\times|\langle N_iJ_im_i|S|N_iJ_im_i\rangle - \langle N_fJ_fm_f|S|N_fJ_fm_f\rangle|^2\ . \qquad \text{(IV.19)}$$

As the approximation (IV.13) may not lead to satisfactory results for small values of N, we shall improve the expression of S as given by the first term of Eq. (IV.14) so that it will be correct to second order in the perturbation potential for all N. This can be done by expanding to second order the first term in Eq. (IV.14) and identifying it with the expression (IV.12).

This allows us to obtain:

$$\eta_{00}(NJm) = \langle NJm|\eta|NJm\rangle\ ,$$

$$A^2_{10}(NJm) = 2(\langle NJm|\eta|NJ+1\,m\rangle^2 + \langle NJm|\eta|NJ-1\,m\rangle^2)\ ,$$

$$A^2_{20}(NJm) = 2(\langle NJm|\eta|NJ+2\,m\rangle^2 + \langle NJm|\eta|NJ-2\,m\rangle^2)\ ,$$

$$A^2_{02}(NJm) = 2(\langle NJm|\eta|N+2\,Jm\rangle^2 + \langle NJm|\eta|N-2\,Jm\rangle^2)\ ,$$

$$A^2_{12}(NJm) = 2(\langle NJm|\eta|N+2J+1\,m\rangle^2 + \langle NJm|\eta|N-2J-1\,m\rangle^2)\ ,$$

$$A^2_{22}(NJm) = 2(\langle NJm|\eta|N+2J+2\,m\rangle^2 + \langle NJm|\eta|N-2J-2m\rangle^2)\ . \qquad \text{(IV.19)}$$

In Hund's b coupling scheme the matrix elements of the phase shift are given by

$$\langle NJm|\eta|N'J'm\rangle = 2\sum_l(-)^{J+J'+1-m+l}\sqrt{(2J+1)(2J'+1)(2N+1)(2N'+1)}\begin{Bmatrix} N & J & 1\\ J' & N' & l\end{Bmatrix}\begin{pmatrix} N & l & N'\\ 0 & 0 & 0\end{pmatrix}\begin{pmatrix} J & l & J'\\ -m & 0 & m\end{pmatrix}$$

$$\times\int_0^\infty\cos(\omega_{NJ,N'J'}t)\,V_l[r(t)]\,dt\ . \qquad \text{(IV.20)}$$

Note that apart from the peaking approximation the S matrix has been calculated exactly to second order and that its property of unitarity is fulfilled.

C. Intermolecular potential and classical trajectory

We use in our calculations an intermolecular potential proposed by Mingelgrin.[19] It is a semiempirical potential, the long range part of which is obtained from the dynamical polarizabilities and the photoionization cross sections of the oxygen molecule. The anisotropy coefficients are determined by analyzing experimental and theoretical results corresponding to various mechanisms in dilute gases. As mentioned above we neglect the internal structure of perturbers so that we write:

$$V(r) = V_0(r) + V_2(r) P_2(\cos\theta) ,$$

with

$$V_0(r) = V_{rep}(r) - V_{att}(r) ,$$

$$V_2(r) = a_r V_{rep}(r) - a_a V_{att}(r) , \qquad \text{(IV.21)}$$

where

$$V_{rep}(r) = \epsilon \left(\frac{\alpha}{6} - 1\right)^{-1} \exp\left[\alpha\left(1 - \frac{r}{r_m}\right)\right], \qquad \text{(IV.22)}$$

$$V_{att}(r) = \epsilon \left(1 - \frac{6}{\alpha}\right)^{-1} \left(\frac{r_m}{r}\right)^6 . \qquad \text{(IV.23)}$$

$\epsilon = 156$ K , $r_m = 3.676$ Å , $\alpha = 19.33$,

$a_a = 0.229$, $a_r = 1.24$.

We have determined the classical trajectories of the relative motion using the isotropic part of the potential and a Romberg numerical procedure. The reduced impact parameter b/r_m was taken from 0.1 to 4 in steps of 0.1, and the reduced kinetic energy $\mu v^2/2\epsilon$ was taken as $z\,2^n$ since the energy dependence of the differential cross section $\sigma(E)$ is large at low energies and small at large energies (cf. Fig. 8). We then calculated the necessary Fourier transforms using a variable step spline integration. Finally the determination of the half-width at half-height of an isolated line is made by carrying out the energy average using a ten point Laguerre integration procedure.

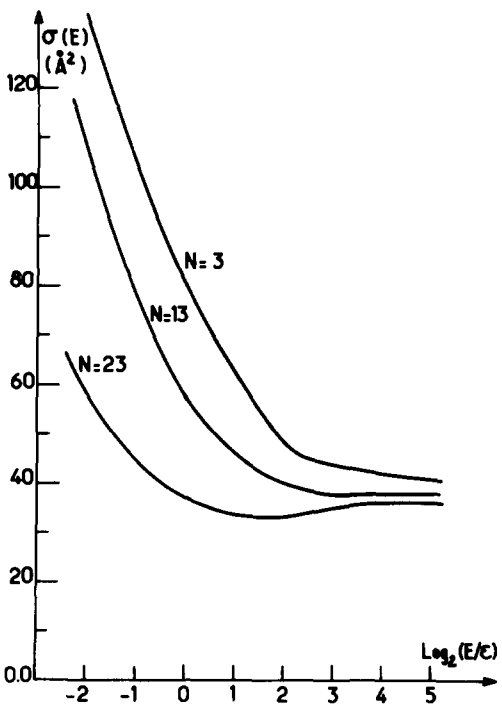

FIG. 8. Energy dependence of the Raman line broadening cross section $\sigma(E)$ for typical values of N, calculated by the present authors and using the potential of Mingelgrin and Gordon (Ref. 19).

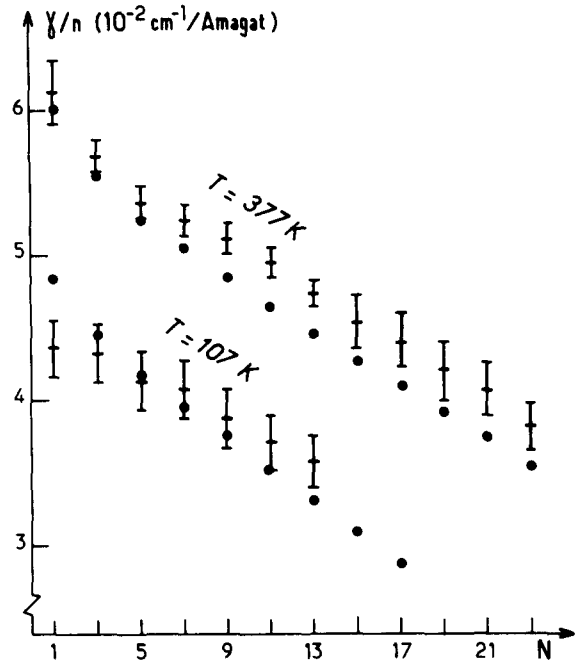

FIG. 9. Self-broadening coefficient for the $N \rightarrow N+2$ rotational Raman transition in oxygen (1 amagat = 2.69 10^{-5} molecule/Å^3). The experimental values are plotted with error bars, for the two extreme temperatures that were studied. The calculated values (•••) were obtained with the Mingelgrin and Gordon potential (Ref. 19).

To compare the results with actual experimental data we synthetized a few triplets $S(N)$ and analyzed them as a real experimental spectrum. We found a half-width which was very close to that obtained by averaging the widths of the individual lines with proper weights. This allowed us to use this simplified procedure to get the theoretical values that will be discussed in the next section.

V. RESULTS AND DISCUSSION

We show in Fig. 9 the experimental and theoretical results for the weighted broadening coefficient that we have obtained for the extreme temperatures that we studied (107 and 377 K). We present in Table III the complete set of experimental and theoretical results.

If we take into account the estimated experimental errors, which are 3% for the most intense lines at room temperature and 8% in the most unfavorable case (large N at low temperature) we find a fairly good overall agreement between experiment and theory. However

TABLE III. Self-broadening coefficients (in 10^{-2} cm^{-1}/amagat) of the rotational Raman transitions $N \rightarrow N+2$ for O_2. The first line gives the experimental value. The second line gives the value calculated with the intermolecular potential of Mingelgrin and Gordon.

N	T (K)	107	115	182	207	234	293	338	366	377
1	expt	4.37	4.41	5.06	5.29	5.46	5.73	5.95	6.08	6.12
	calc	4.83	4.89	5.24	5.34	5.44	5.67	5.84	5.95	6.01
3	expt	4.33	4.36	4.89	4.97	5.14	5.36	5.54	5.63	5.69
	calc	4.45	4.50	4.82	4.92	5.02	5.24	5.40	5.51	5.55
5	expt	4.13	4.16	4.57	4.72	4.81	5.05	5.17	5.28	5.36
	calc	4.18	4.22	4.53	4.63	4.73	4.95	5.11	5.21	5.25
7	expt	4.07	4.08	4.47	4.55	4.66	4.90	5.09	5.15	5.24
	calc	3.96	4.00	4.31	4.41	4.51	4.74	4.91	5.01	5.05
9	expt	3.87	3.97	4.35	4.43	4.54	4.79	5.00	5.07	5.12
	calc	3.75	3.79	4.10	4.20	4.31	4.54	4.71	4.81	4.85
11	expt	3.71	3.77	4.16	4.32	4.46	4.57	4.80	4.89	4.96
	calc	3.53	3.57	3.88	3.99	4.10	4.31	4.51	4.61	4.66
13	expt	3.58	3.65	3.96	4.03	4.16	4.42	4.60	4.67	4.74
	calc	3.32	3.35	3.67	3.77	3.88	4.12	4.30	4.41	4.46
15	expt		3.45	3.70	3.88	3.99	4.16	4.34	4.48	4.53
	calc		3.13	3.45	3.56	3.67	3.92	4.11	4.23	4.27
17	expt		3.31	3.54	3.68	3.78	4.01	4.24	4.33	4.40
	calc		2.91	3.24	3.35	3.47	3.74	3.93	4.05	4.10
19	expt			3.37	3.51	3.59	3.78	3.98	4.13	4.21
	calc			3.02	3.14	3.27	3.55	3.75	3.87	3.92
21	expt				3.35	3.42	3.62	3.84	4.02	4.07
	calc				2.92	3.06	3.35	3.56	3.68	3.74
23	expt						3.47	3.65	3.76	3.82
	calc						3.14	3.36	3.49	3.54
25	expt						3.26	3.47	3.61	3.66
27	expt						3.06	3.32	3.36	3.42

there exists an almost constant difference between experiment and theory, the calculated values being systematically smaller than the experimental ones by an amount larger than their estimated accuracy. Note that these differences show up most clearly for low values of N and at low temperature.

This may be due either to neglecting systematic errors in our data analysis, to improper approximations in the theory, or to an inadequate potential. We shall first discuss how changes in the potential affect the theoretical linewidths and thus we shall make some comments about the approximations in the theory.

We have studied the sensitivity of the theoretical broadening coefficients to the different parameters of the Buckingham potential. First we varied the coefficient α in Eqs. (IV.22) and (IV.23). This corresponds to a change in the repulsive isotropic and anisotropic potential, so that it has a direct influence both on the classical trajectories and on the phase shifts. We plot in Fig. 10 the results of these calculations along with the experimental data. We find that small α coefficients lead to a large N dependence of the theoretical results. To get the right slope of γ vs N we found that we had to increase α compared to the value taken by Mingelgrin

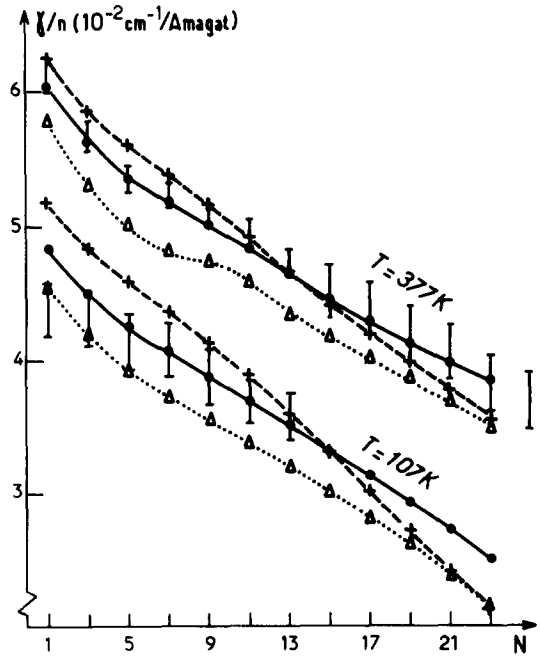

FIG. 10. Optimization of the fit to the experimental values of the self-broadening coefficient in oxygen. We have varied the α coefficient in the Mingelgin–Gordon potential (Ref. 19); $\alpha = 16$ (+) $\alpha = 22$ (Δ). Then for $\alpha = 22$ we chose $a_r = 1.55$ (• • •).

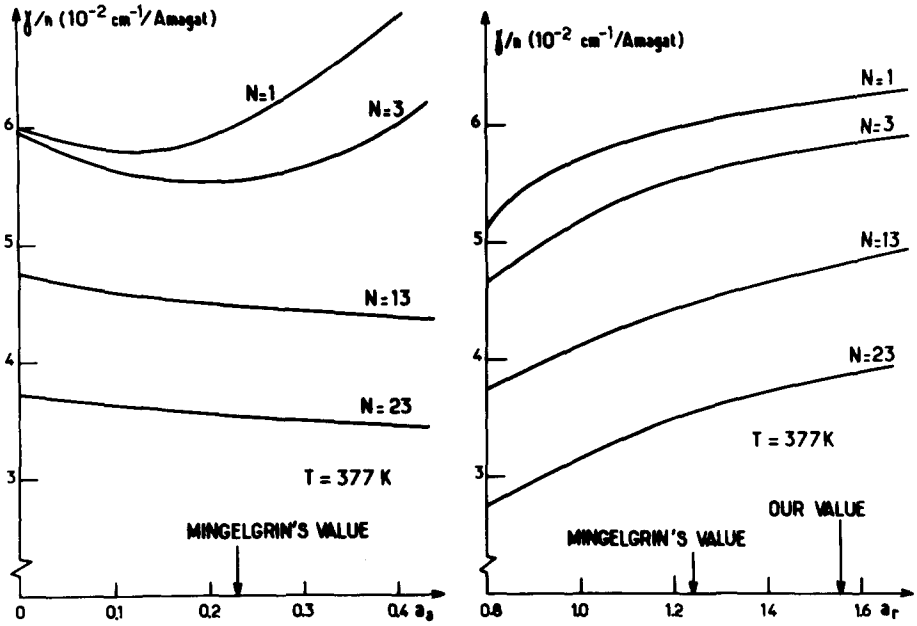

FIG. 11. Dependence of the self-broadening coefficients with respect to the parameters of the anisotropic potential (a): to the attractive part (a_a). (b): to the repulsive part (a_r). This shows that except for small N, the repulsive potential plays the dominant role.

and obtain for $\alpha = 22.0$ a good agreement except for a constant vertical shift to be discussed later. Note that the influence of α is best seen for the highest temperature where the experimental errors are less important and where the repulsive wall plays an important role in the broadening phenomenon.

We then studied the effect of changing the strength of the anisotropic potential. We show in Fig. 11 the variations of the calculated broadening coefficient with respect to the repulsive anisotropic parameter a_r and to the attractive anisotropic parameter a_a. We have indicated in the figures the values of Mingelgrin[19] by vertical lines. We note differences in the sensitivity of the broadening coefficient to these parameters. Except for small rotational quantum numbers, it appears that the broadening coefficients are more sensitive to the repulsive coefficient a_r than to the attractive one a_a, and that this behavior is more pronounced when the temperature is increased. This confirms the fact that the repulsive anisotropic potential plays a dominating role for the collisional broadening of the lines, as was already found in CO_2 using more primitive calculations.[36]

We shall discuss these results. For this purpose, we shall consider the two parts of the expression (IV.17). For all transitions our calculations show that γ^{el} is less than 4% of the total linewidth. This means that pure phase shift effects are almost negligible and that we can describe the results simply in terms of lifetimes of molecular levels, which in our notation are related to the inverse of the inelastic contributions γ^{in} in Eq. (IV.17). Following Eqs. (IV.14), (IV.19), and (IV.20) we shall now consider the power spectral density of the perturbation potential treating separately the attractive and repulsive parts.

Due to its long range the attractive potential leads to a fairly narrow power spectral density, whereas the repulsive potential leads to a broad spectrum due to the very fast variation of $V_{rep}[r(t)]$. As the broadening of the line N is related to the power density of the collisional noise at a frequency of the order of $(4N+6)B$, we expect that the attractive potential will influence just the small N lines whereas all lines will be sensitive to the repulsive potential. As indicated above, this can be seen in Fig. 11(a) showing the great sensitivity of the half-widths of the lines with respect to the coefficient a_a of the attractive potential for small N. On the contrary, Fig. 11(b) shows a large dependence of all half-widths when the repulsive potential coefficient a_r is changed.

One can therefore derive new values of α, a_r, and a_a from the experimental data by the following procedure. Starting from the initial $a_a = 0.214$ we choose α and a_r to get a good fit of the half-widths for large N and at various temperatures. This leads to $\alpha = 22.0$ and $a_r = 1.55$. We then found that it was not necessary to look for a new a_a as we already have good overall agreement between calculated and experimental results (see Fig. 10) at least within experimental errors.

Obviously our theoretical results include errors which are due to the several approximations that we have made. Let us recall these: neglect of rotational motions of the perturbers (as we work here in pure oxygen), semiclassical approximation, peaking approximation, and simplification of the phase shift [Eq. (IV.13)].

When the same potential is used in a classical calculation, as performed by Mingelgrin and Gordon,[19] the corresponding linewidths are larger than ours as is shown in Table IV. The differences are probably not due to the peaking approximation if we refer to previous calculations[37] of correlations functions of $P_l(\cos\theta)/r^n$ for Lennard-Jones trajectories, and various values of l and n. It was found that $C(0)$, which is the integrated

TABLE IV. Comparison of the theoretical broadening cooefficients (in 10^{-2} cm^{-1}/amagat) calculated by Mingelgrin and Gordon[a] and by the present authors.

N	Ref. 29	Present work
7	5.28	4.74
9	5.26	4.54
11	5.15	4.31
13	4.65	4.12
15	4.74	3.92

[a]Reference 19.

power spectrum of the collisional noise, does not depend on l, as can be seen in Table I of Ref. 37 after proper normalization $[(2l+1)]$. However the correlation time decreases when l increases, but by a relative quantity that decreases rapidly when n increases. Here we are dealing with a very short range repulsive potential so that we do not expect much difference in the corresponding correlation times for $l=0$ or $l=2$. This allows us not to use the elaborate calculations of Neilsen and Gordon,[38] where the time dependence of θ is taken into account. We believe that we can refer to this same work[38] to justify the semiclassical approach.

Now we have considered the oxygen perturber as a structureless particle. This approximation will be tested in a future paper where we shall compare experimental data for O_2–argon collisions with the present theory and that of Mingelgrin and Gordon.[19] However we can again use the fact that repulsive forces are dominant to neglect resonance effects in O_2–O_2 collisions which might play a role for the most populated rotational levels.[14]

CONCLUSION

In this paper we have presented extended measurements of rotational Raman line pressure broadening in pure oxygen. Using an elaborate experimental setup and efficient data reduction we obtain accurate experimental results. We have then compared this data with the values computed using a semiclassical theory which is not perturbative even though approximations have to be made. Starting from a previously published intermolecular potential we obtain calculated values that are systematically somewhat smaller than the experimental ones. We then propose to change the parameters of the intermolecular potential and obtain a very good agreement. This new potential involves a reduction of the range of the repulsive potential.

Finally in a discussion of the results we have shown that the repulsive part of the anisotropic potential plays a dominant role in order to reproduce the slow reduction of the linewidths when the rotational quantum number increases. In order to test in more detail the present model we shall present later experimental results for oxygen in rare gases and other diatomics.

ACKNOWLEDGMENT

The computer time made available by the Centre de Calcul of the Laboratoire d' Astronomie spatiale of Marseille is gratefully acknowledged.

[1]For a review of theoretical approaches on the subject, see, for example, *Atom–Molecule Collision Theory*, edited by R. B. Bernstein (Plenum, New York, 1979).
[2]M. Faubel and J. P. Toennies, in *Advances in Atomic and Molecular Physics*, edited by D. R. Bates and B. Bederson (Academic, New York, 1977), Vol. 13, p. 229.
[3]See, for example, J. O. Hirschfelder, C. F. Curtiss, and R. B. Bird, *Molecular Theory of Gases and Liquids* (Wiley, New York, 1967).
[4]K. F. Herzfeld and T. A. Litovitz, *Absorption and Dispersion of Sound Waves* (Academic, New York, 1965).
[5](a) R. A. J. Keijser, K. D. van den Hout, M. de Groot, and H. F. P. Knaap, Physica 76, 515 (1974); (b) R. A. J. Keijser, K. D. van den Hout, and H. F. P. Knaap, Physica 76, 577 (1974); (c) A. F. Turfa and H. F. P. Knaap, Chem. Phys. 62, 57 (1981).
[6]P. G. van Ditzhuyzen, L. J. F. Hermans, and H. F. P. Knaap, Physica A 88, 452 (1977).
[7](a) F. Baas, J. N. Breunese, H. F. P. Knaap, and J. J. M. Beenakker, Physica A 88 (1977); (b) F. Baas, J. N. Breunese, and H. F. P. Knaap, Physica A 88, 34 (1977); (c) F. Baas, P. Oudeman, H. F. P. Knaap, and J. J. M. Beenakker, Physica A 88, 44 (1977).
[8]H. Rabitz, *Annual Review of Physical Chemistry* (Annual Reviews, Palo Alto, 1974), Vol. 25, p. 155.
[9]D. Robert in *Raman Spectroscopy Linear and Nonlinear*, edited by J. Lascombe and P. V. Huong (Wiley, Chichester, 1982), pp. 269–284.
[10]T. W. Meyer and C. K. Rhodes, Phys. Rev. Lett. 32, 637 (1974).
[11]S. L. Dexheimer, M. Durand, T. A. Brunner, and D. E. Pritchard, J. Chem. Phys. 76, 4996 (1982).
[12]G. C. Maitland, M. Rigby, E. B. Smith, and W. A. Wakehan, *Intermolecular Forces* (Oxford Clarendon, Oxford, 1981).
[13]E. W. Smith, M. Giraud, and J. Cooper, J. Chem. Phys. 65, 1256 (1976); 66, 376 (1977).
[14]C. G. Gray and J. van Kranendonk, Can. J. Phys. 44, 2411 (1966).
[15]E. W. Smith and M. Giraud, J. Chem. Phys. 71, 4209 (1979).
[16]G. Herzberg, *Spectra of Diatomic Molecules*, 2nd ed. (Van Nostrand, Princeton, 1963), pp. 130–132.
[17]R. A. J. Keijser, J. R. Lombardi, K. D. van den Hout, B. C. Sanctuary, and H. F. P. Knaap, Physica 76, 585 (1974).
[18]K. S. Jammu, G. E. St. Johns, and H. L. Welsh, Can. J. Phys. 44, 797 (1966).
[19]U. Mingelgrin and R. G. Gordon, J. Chem. Phys. 70, 3828 (1979).
[20]G. Placzeck and E. Teller, Z. Phys. 81, 209 (1933).
[21]G. Herzberg, *Spectra of Diatomic Molecules*, 2nd ed. (Van Nostrand, Princeton, 1963), pp. 130–132.
[22]K. Altmann, G. Stray, J. G. Hochenbleicher, and J. Brandmuller, Z. Naturforsch. 27, 56 (1972).
[23]M. Berard and P. Lallemand, Opt. Commun. 30, 175 (1979).
[24]H. J. Liebe, G. G. Gimmestad, and J. D. Hopponen, IEEE Trans. Antennas Propag. AP 25, 327 (1977).
[25]J. W. Nibler and G. V. Knighten, in *Raman Spectroscopy of Gases and Liquids*, edited by A. Weber (Springer, Berlin, 1979), Chap. VII.
[26]D. Fabre, G. Wildenlocher, and H. Vu, Opt. Commun. 4, 421 (1972).
[27]M. Berard, J. Phys. E (to be published).
[28]J. P. Cebe, M. Giraud, and E. W. Smith, Chem. Phys. Lett. 81, 37 (1981).
[29]M. Berard and P. Lallemand, C. R. Acad. Sci. Paris 294,

1167 (1982).
[30]F. Barocchi, P. Mazzinghi, and M. Zoppi, Phys. Rev. Lett. **41**, 1785 (1978).
[31]M. Boulet, D. Robert, and L. Galatry, J. Chem. Phys. **72**, 751 (1980).
[32]R. G. Gordon, Adv. Magn. Reson. **3**, 1 (1968).
[33]U. Fano, Phys. Rev. **131**, 259 (1963).
[34]K. S. Lam, J. Quant. Spectrosc. Radiat. Transfer **17**, 351 (1977).
[35]R. P. Srivastava and H. R. Zaidi, in *Raman Spectroscopy of Gases and Liquids*, edited by A. Weber (Springer, Berlin, 1979), Chap. V.
[36]M. C. Herpin and P. Lallemand, J. Quant. Spectrosc. Radiat. Transfer **15**, 779 (1975).
[37]M. Berard and P. Lallemand, J. Quant. Spectrosc. Radiat. Transfer **19**, 387 (1978).
[38]W. Neilsen and R. G. Gordon, J. Chem. Phys. **58**, 4131, 4149 (1973).